INERTIA CONTROLLED INSTABILITY AND SMALL SCALE STRUCTURES OF SHEET AND CLOUD CAVITATION

Steffen J. Schmidt, Matthias Thalhamer, Günter H. Schnerr
Technische Universität München - Fachgebiet Gasdynamik
Boltzmannstr. 15, D-85748 Garching, Germany
schmidt@flm.mw.tu-muenchen.de, http://www.lhm.mw.tu-muenchen.de/gd/

ABSTRACT
The present investigation focuses on the numerical simulation of inertia driven dynamics of 3-D sheet and cloud cavitation on a 2-D NACA 0015 hydrofoil. Special emphasis is put on the numerical analysis of the re-entrant flow, the break-up of the sheet cavity and the formation of clouds. We demonstrate that our CFD-Tool **CATUM** (**CA**vitation **T**echnische **U**niversität **M**ünchen) is able to predict even delicate 3-D flow features such as irregular break-up patterns, cavitating hairpin and horseshoe vortices, 3-D instabilities in spanwise direction and the formation and propagation of shocks due to collapsing clouds close to the trailing edge of the hydrofoil. The numerically predicted flow features agree well with the experimental observations of Kawanami et al [1].

INTRODUCTION
Kawanami et al [1] investigate the 3-D structure of the cavitating flow around a NACA 0015 hydrofoil with cord length l_{cord}=0.08 m and span l_{span}=0.15 m. The hydrofoil is placed within a rectangular test section, the angle of attack is 8.36°. They observe that the dimensionless spanwise length $l_{cav,s}/l_{cord}$ of the clouds is roughly proportional to the dimensionless length $l_{cav,c}/l_{cord}$ of the sheet cavity along the cord of the hydrofoil. Furthermore, they show the formation and shedding of multiple clouds if $l_{cav,c}<<l_{span}$ (**Fig. 1**). An interesting situation arises at the region of $l_{cav,c}/l_{cord}>0.5$, where Kawanami et al observe irregular break-up patterns. If $l_{cav,c}/l_{cord}\approx1$, then the irregular pattern is replaced by the shedding of one single cloud that covers the full width of the test section. Franc [2] refers the previously stated 3-D aspects of cloud shedding as being intrinsic instabilities - often referred as self-excited instabilities. Although the width of the test section might influence the characteristics of multiple shedding and irregular break-up, the physical origin of these instabilities seems to be determined by the cavity itself. It is known that the basic shedding mechanisms - the formation of re-entrant flow, the resulting separation of the sheet cavity, the formation of a downstream traveling spanwise vortex and the subsequent break-up into numerous cloudy structures - are mainly inertia controlled [3]. **The aim of this investigation is to demonstrate that the occurrence of irregular break-up patterns and of 3-D spanwise instabilities is essentially inertia controlled as well**. The key idea is to focus exclusively on the inviscid dynamics of cavitating flows by means of numerical simulation. This allows distinguishing inertia driven instabilities from instabilities due to viscosity/turbulence.

PHYSICAL MODEL
It is known that highly purified water can reach significant metastable thermodynamic states including tension [4]. The classical nucleation theory predicts that homogeneous nucleation is negligible for the typically arising flow conditions within hydraulic machinery. It is widely accepted that flow induced evaporation - cavitation - is dominated by heterogeneous processes such as the growth of liquid embedded gas bubbles [5]. Provided that the number density and the average size of heterogeneous nuclei are sufficiently large, the onset of evaporation occurs close to the saturation conditions defined by the Clausius-Clapeyron relation. Concerning natural (unpurified) water as working fluid within large scale hydraulic machinery, it is reasonable to neglect metastable thermodynamic conditions and to assume stable thermodynamic conditions exclusively. This assumption is questionable for operating conditions close to cavitation inception, yet it is sophisticated for sufficiently developed cavitating flow such as the investigated sheet and cloud cavitation. If we consider an open thermodynamic system at one instant in time $t=t_1$ with given total mass $m(t_1)$, total internal energy $U(t_1)$ and fixed volume V, then the fundamental laws of thermodynamics imply that the only stable thermodynamic state is the equilibrium state, denoted by the subscript "eq". It follows that the pressure $p_{eq}(t_1)$, the temperature $T_{eq}(t_1)$ and the mass specific Gibbs energy $g_{eq}(t_1)$ are spatially and temporally constant within the specified thermodynamic system. Moreover, the system has minimal total Gibbs energy $G_{eq}(t_1)$ and maximal total entropy $S_{eq}(t_1)$. This information provides a unique and complete specification of the thermodynamic state including the phase properties (e.g. the mass fractions of liquid and vapor) of the system at time instant $t=t_1$. The previous consideration is the thermodynamic basis for modeling and simulation of cavitating flows due to the following aspects.
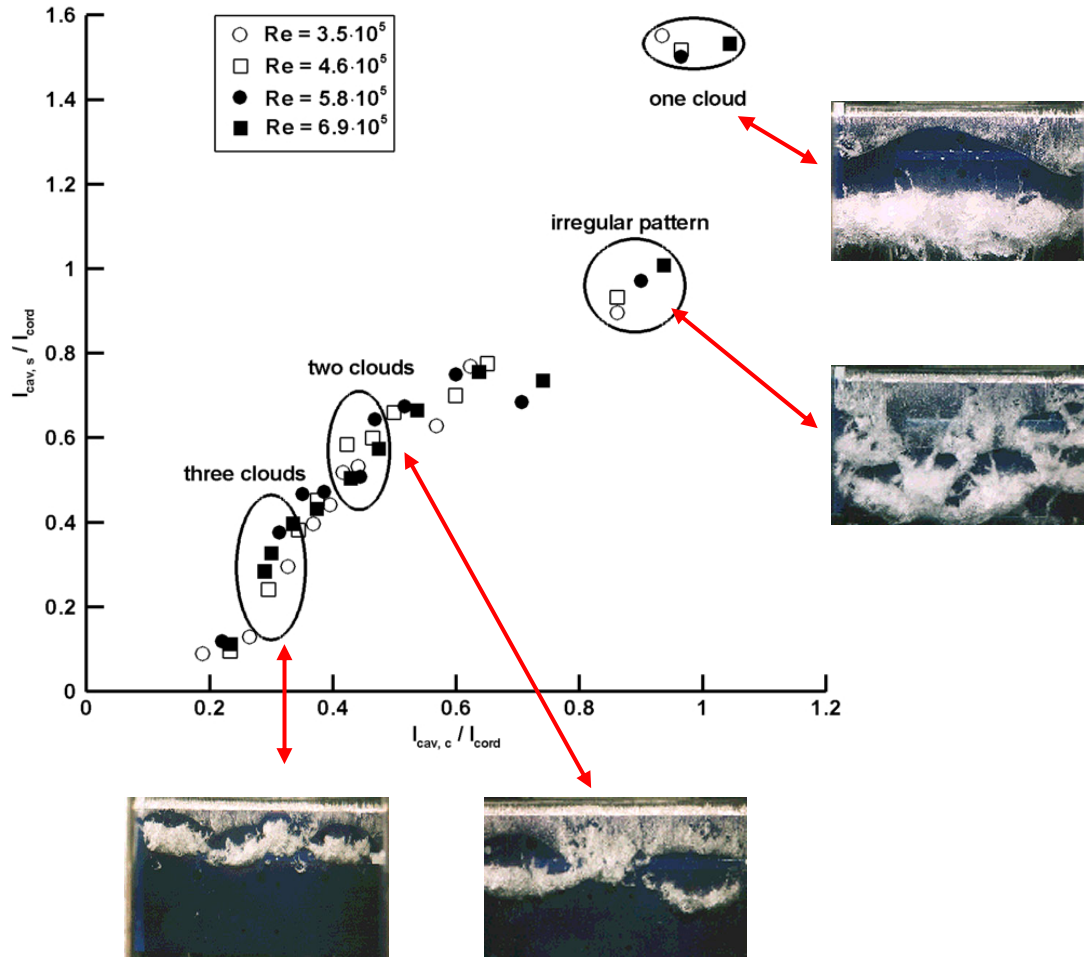
Fig. 1 **Multiple shedding of clouds on a 2-D NACA 0015 hydrofoil**
The arising cloud patterns show a correlation of the length $l_{cav,c}$ of the cavity along the cord with the spanwise length $l_{cav,s}$ of the shedded clouds. For $l_{cav,c}/l_{cord} \approx 0.8$ irregular break-up is observed, for $l_{cav,c}/l_{cord} \approx 1.0$ a single cloud is shedded.
NACA 0015, l_{cord}=0.08 m, l_{span}=0.15 m, 8.36° angle of attack, u_{in}=6.0 m/s -12 m/s, $T_{in} \approx$299 K, Re_c=3.5·10^5 - 6.9·10^5, σ_{ref}=1.05 - 2.13, fluid water/water vapor.
The experiments indicate that the arising structures are independent of the Reynolds number.
Experiments and data from [1], reproduced with permission from Hajime Yamaguchi.

1) If the numerical method is a finite volume method, then the derivation of the stable thermodynamic state within each finite volume follows exactly the previously described consideration for each instant in time. The spatial resolution of the model is then consistent with the spatial resolution of the numerical approach, which is defined by the size of the finite volumes.
2) The phase properties are directly obtainable from the total mass and the total internal energy U within each finite volume. Contrary to other models, the thermodynamic model does neither require the specification of (unknown) parameters nor does it require the formulation and solution of additional transport equations.
3) The model takes compressibility effects into account. This is necessary for simulation of shock formation and propagation.

4) The model is applicable to simulate saturated mixtures as well as pure vapor sheets and pure liquid flow.
5) If the model is combined with a conservative numerical algorithm (conservative Euler solver), then the combination of both provides a mathematically well posed hyperbolic problem where the speed of sound is implicitly defined by the equilibrium speed of sound c_{eq}.
6) The model includes the effects of the latent heat due to phase transition.
As our major interests are intrinsic instabilities of wave and inertia driven flows the governing equations are the 3-D compressible time dependent Euler equations. Several experimental and numerical investigations show that the dynamics of developed cavitating flow is only weakly dependent on the Reynolds number (see **Fig. 1**). Presuming that

the boundary layers of the investigated flow remain attached as long as phase transition does not occur, the inviscid treatment of the fluid leads to suitable physical models that can be simulated significantly more efficient and more accurate than viscous fluids. However, the inclusion of viscous effects within the model is possible.

Let $\bar{q}$ be the vector of conserved quantities composed by the density ρ, the components u_i of the velocities in coordinate direction x_i and the specific total energy E as the sum of the specific internal energy e per unit mass and the specific kinetic energy $0.5 \cdot \sum (u_i)^2$. Let $F_i(\bar{q})$ be the physical flux in coordinate direction x_i, while δ_{ij} and p denote the Kronecker symbol and the pressure respectively

$$\bar{q} = \begin{pmatrix} \rho \\ \rho u_1 \\ \rho u_2 \\ \rho u_3 \\ \rho E \end{pmatrix}, \quad F_i(\bar{q}) = \rho u_i \cdot \begin{pmatrix} 1 \\ u_1 \\ u_2 \\ u_3 \\ E \end{pmatrix} + p \cdot \begin{pmatrix} 0 \\ \delta_{1i} \\ \delta_{2i} \\ \delta_{3i} \\ u_i \end{pmatrix}. \tag{1}$$

The differential or pointwise form of the Euler equations can be written as

$$\frac{\partial}{\partial t} \bar{q} = -\sum_{i=1}^{3} \frac{\partial}{\partial x_i} F_i(\bar{q}). \tag{2}$$

Instead of enforcing the conservation principles in a pointwise fashion we use the weak form of the Euler equations. Therefore, we partition the flow domain into disjoint fixed control volumes C_k of a corresponding volume V_k, a surface S_k and an outer unit normal vector $\bar{n}_k = (n_{k,1} \ n_{k,2} \ n_{k,3})^t$. The weak form of the Euler equations for each control volume C_k follows as

$$\frac{d}{dt} \int_{C_k} \bar{q} dV_k = -\int_{S_k} \sum_{i=1}^{3} n_{k,i} F_i(\bar{q}) dS_k. \tag{3}$$

By defining the cell average operator A_k

$$A_k(\bar{q}) := \frac{1}{V_k} \int_{C_k} \bar{q} dV_k, \tag{4}$$

we assign to all weak solutions within the cell C_k their common integral average value $\bar{q}_k = A_k(\bar{q})$. It turns out that the weak form of the Euler equations resembles a system of evolution equations of the cell averages of weak solutions

$$\frac{d}{dt} \bar{q}_k = -\int_{S_k} \sum_{i=1}^{3} n_{k,i} F_i(\bar{q}) dS_k. \tag{5}$$

The closure of the defined initial-boundary value problem (5) necessitates constitutive relations for the thermodynamic

quantities ρ_k, e_k, p_k as well as consistent initial and boundary conditions. In this section we assume that consistent initial and boundary data are available. Thus, the physical fluxes along the boundary surfaces are known and hence, equation (5) reduces to an initial value problem. At each instant in time and for each control volume C_k the known values $\bar{q}_k$ determine the average density ρ_k, velocity $\bar{u}_k$ and total energy E_k within the control volume C_k. Therefore, the average specific internal energy e_k is known as well. We now follow the thermodynamic considerations stated at the beginning of this section by interpreting each control volume C_k at each instant in time as an open thermodynamic system with known total mass m_k, total internal energy U_k and fixed volume V_k. In order to obtain the stable thermodynamic states p_{eq} and T_{eq} from the known conditions we relate them by suitable equations of state. The most accurate database for the thermodynamic properties of water, water vapor and saturated mixtures of water and water vapor is the IAPWS - International Association for the Properties of Water and Steam - database. They provide "state of the art" equations of state, so called reference equations of state [6]. Although it is possible to apply these equations to determine the unknown thermodynamic properties, we prefer to use suitable approximate equations. The reason therefore is given by the fact that the evaluation of the IAPWS equations is enormously time consuming. Although our approximate equations are significantly more efficient then the IAPWS equations, they are still highly accurate within the relevant thermodynamic regime of the considered flow. Following an idea of Saurel et al. [7], we distinguish the following three cases.

Case 1) The stable thermodynamic state corresponds to a **pure liquid state**. Here, we apply a modified Tait model

$$\frac{p_k + B}{p_{sat}(T_k) + B} = \left(\frac{\rho_k}{\rho_{l,sat}(T_k)} \right)^N \tag{6}$$

to relate the pressure p_k to the density ρ_k and the temperature T_k of the liquid. The temperature T_k is obtained by a caloric equation that relates the known specific internal energy e_k to the unknown temperature T_k. Even though the temperature variation of the liquid is typically small, the modification of the Tait equation remains necessary in order to ensure a continuous connection of the Tait model to the temperature dependent saturation conditions - see case 2). For water we use the constants B=3300 bar and N=7.15.

Case 2) The stable thermodynamic state corresponds to a **saturated mixture of water and water vapor**. The stable coexistence of both phases implies that the pressure p_k is determined by the Clausius-Clapeyron relation and the average density ρ_k within each cell C_k is a convex combination of the saturation densities $\rho_{l,sat}$, $\rho_{v,sat}$ of liquid and vapor. The temperature T_k is a function of the mass specific internal

energy e_k. By defining the vapor volume fraction α_k and the vapor mass fraction ε_k we obtain the unknown quantities T_k, α_k, ε_k and p_k as unique solutions of the system

$$\rho_k = \alpha_k \cdot \rho_{v,sat}(T_k) + (1-\alpha_k) \cdot \rho_{l,sat}(T_k) \tag{7}$$

$$e_k = \varepsilon_k \cdot e_{v,sat}(T_k) + (1-\varepsilon_k) \cdot e_{l,sat}(T_k) \tag{8}$$

$$\varepsilon_k \cdot \rho_k = \alpha_k \cdot \rho_{v,sat}(T_k) \tag{9}$$

$$p_k = p_{sat}(T_k) \tag{10}$$

$$0 < \alpha, \varepsilon < 1 . \tag{11}$$

Thereby, the incorporated temperature dependent saturation conditions are modeled by the Oldenbourg polynomials [8].

Case 3) The stable thermodynamic state corresponds to a **pure vapor state**. Here, the applied constitutive relation models pure vapor as calorically perfect gas, where the ratio of the specific heats is given by $\kappa = 1.327$ and the specific gas constant is 461.5 J/kg K.

The comparison of the described thermodynamic closure relations with respect to the IAPWS data [6] demonstrates that the relations accurately model the behavior of water and water vapor for a large range of thermodynamic subcritical conditions, especially for the temperature range of $283 \text{ K} \le T \le 350 \text{ K}$.

NUMERICAL METHOD

The CFD-Tool **CATUM** (**CA**vitation **T**echnische **U**niversität **M**ünchen) is based on a semi-discrete unsplit finite volume method that operates on block structured meshes. The spatial discretization is obtained by a modified flux function that enables time accurate simulations of compressible high and low Mach number flows including wave dynamics and shock propagation [9]. We apply non-linear reconstruction procedures (TVB, TVD) to the primitive variables and obtain 2nd order accurate approximations of smooth quantities as well as sharp representations of discontinuous flow features. The temporal discretization is obtained by a 2nd order accurate explicit 4-stage Runge-Kutta method with enlarged stability region. Our CFD-Tool **CATUM** relies on an approximate solution of the evolution equation (5) for each control volume C_k. The thermodynamic model is given by the constitutive relations (6)-(11). By replacing the physical fluxes $F(\bar{q})$ in Eq. (5) with the numerical fluxes $F(\bar{q}^*)$, we obtain a set of ordinary differential equations, which represent a semi-discrete unsplit finite volume method for hexahedral volumes

$$\frac{d}{dt}\bar{q}_k = -\sum_{i=1}^{6} S_{k,i} \cdot F(\bar{q}^*) . \tag{12}$$

For presentation purposes we assume that $\bar{q}_k$ and $\bar{q}_i$ are the average conserved quantities within two adjacent control volumes C_k, C_i and let $S_{k,i}$ be the shared surface $S_{k,i} = C_k \cap C_i$ which is supposed to be perpendicular to the x_1 spatial direction. We further assume that the x_1 spatial direction increases from C_k to C_i. Hence, the required flux is the approximate flux $F_1(\bar{q})$ in x_1 spatial direction. Provided that the flow is subsonic, the approximate states $\bar{q}^*$ at the shared surface are obtained by the following procedure. The approximate velocity u_1^* is given by

$$u_1^* := \frac{u_{1,k} + u_{1,i}}{2} + \frac{2 \cdot (p_k - p_i)}{\rho_k \cdot c_k + \rho_i \cdot c_i} . \tag{13}$$

The pressure p_k, the density ρ_k, the speed of sound c_k and the $u_{1,k}$ velocity component correspond to the cell average values within cell C_k, otherwise the values correspond to cell C_i. Equation (13) can be interpreted as an approximate solution for the resulting velocity of the associated Riemann problem between cells C_k and C_i. A detailed derivation of Eq. (13) based on the theory of characteristics was recently published (Schmidt et al [10]). The pressure p^* at the shared surface is defined by

$$p^* := \frac{p_k + p_i}{2} . \tag{14}$$

Assuming that the value of u_1^* as defined by Eq. (13) is positive, the upwind character of the discretization is obtained by defining the remaining quantities at the shared surface as

$$\rho^* := \rho_k, \quad u_2^* := u_{2,k}, \quad u_3^* := u_{3,k}, \quad E^* := E_k. \tag{15}$$

Otherwise, if u_1^* as defined by Eq. (13) is negative, the subscripts k in Eq. (15) are replaced by i. With these definitions the numerical fluxes are completely defined. In contrast to classical numerical flux functions the proposed numerical flux is consistent with respect to the asymptotic behavior of the governing equations for $M \to 0$. Therefore, the novel method enables the simulation of low Mach number flows including wave dynamics without the well known draw backs of classical schemes as stated in the introduction part of this investigation. The consistency with respect to $M \to 0$ is achieved by Eq. (14) which defines the pressure p^* at the shared surface as the arithmetic mean of the pressure within the adjacent cells. The proposed flux function is replaced by pure upwinding of all quantities if the flow is locally supersonic. In order to ensure high resolution of discontinuities such as shocks and contact waves we apply the minmod TVD-limiter to reconstruct the density field and the WENO-3 procedure to reconstruct the velocity field. This choice is based on the observation that the density field requires a monotone

reconstruction procedure in order to avoid oscillations in regions of large gradients, especially in regions where evaporation/condensation takes place.

The temporal discretization is obtained by a 4-stage Runge-Kutta method. The 2nd order accurate low-storage time discretization for cell C_k is given by

$$\vec{q}_k^0 := \vec{q}_k(t_0), \quad \vec{q}_k^i := \vec{q}_k^0 - \alpha_i \cdot \frac{\Delta t_{CFD}}{V_k} \cdot D_s(\vec{q}^i), \qquad (16)$$

$$\vec{q}_k(t_0 + \Delta t_{CFD}) := \vec{q}_k^4 \qquad (17)$$

Here, the expression $D_s(\vec{q}^i)$ corresponds to the spatial discretization as given by Eq. (12). In order to optimize the stability region of the method, numerical stability tests have been performed. The resulting coefficients $\alpha_{i=1...4}$ are $\alpha_1 = 0.11$, $\alpha_2 = 0.2766$, $\alpha_3 = 0.5$ and $\alpha_4 = 1.0$ which enable stable time integration for CFL-numbers up to 2.0. A detailed description of the CFD-Tool **CATUM** including validation examples is given by Schmidt et al. [10]. The derivation of weakly reflective boundary conditions for simulation of wave dynamics within cavitating flows is given by Schnerr et al. [11]. The numerical analysis of cavitating flows within fuel injection nozzles and around profiles of propeller blades are published by Schmidt et al.[12,13] and Sezal et al.[14].

NUMERICAL RESULTS

We simulate the cavitating flow around a 2-D NACA 0015 hydrofoil (angle of attack 6°, cord length l_{cord}=0.13 m, span width l_{span}=0.3 m) that is placed in the middle of a rectangular test section (height 0.3 m, depth 0.3 m, length 0.9 m). The walls of the test section and the surface of the hydrofoil are modelled as inviscid adiabatic walls. At the inlet of the numerical domain the velocity u_{in}=30 m/s and the static temperature T_{in}=293 K of the pure liquid inflow are prescribed.

At the outlet we apply an asymptotic boundary condition for the static pressure p_{exit}=4.5 bar. The resulting cavitation number is σ_{ref}=1.0. The numerical domain is discretized by $2 \cdot 10^5$ cells (coarse grid G1), $4 \cdot 10^5$ cells (medium grid G2), $3 \cdot 10^6$ cells (fine grid G3) and $2.4 \cdot 10^7$ cells (finest/target grid G4). All computational grids are structured multi-block hexahedral grids. Let Δx be the characteristic length of the smallest computational cell, then the numerical time step is necessarily of the order of $\Delta t_{CFD} \sim \Delta x / c_l$, where c_l is the speed of sound of pure liquid. Hence, the numerical time step Δt_{CFD} and the characteristic length Δx are directly related. The finest grid (target grid) used for this investigation leads to the characteristic length $\Delta x \approx 0.4$ mm of the smallest cells, which is at least one order of magnitude larger than the radius of a typical micro-bubble and definitely one order of magnitude larger than the Taylor microscale, which provides an indication of the minimum length scale on which inertia effects are still dominant over viscous effects. The resulting numerical time step for the finest grid is $\Delta t_{CFD,fine}$=8.5·10^{-8}s. These small numerical time steps are necessary to resolve wave dynamics such as shock formation and propagation. In order to accelerate the numerical simulation we apply a grid sequencing technique. At first, a simulation on the coarse gird is performed until the typical periodic shedding of the cavitating flow is observed. To determine the shedding frequency we analyse the integrated vapor volume content V_{vap} [%] within the computational domain. **Figure 2** depicts the temporal evolution of V_{vap} during the simulated time interval of $\Delta t_{sim} \approx 0.25$ s. The simulated time interval Δt_{coarse}=0.15 s on the coarse grid corresponds to approximately 17 shedding cycles. This time interval is sufficient to ensure that the disturbances due to the initialization of the flow field are no longer present. As the minimum cell size of the coarse grid is significantly larger than the one of the target grid, the numerical time step is larger as well. Additionally, the number of evolution equations (5) is by 2 orders of magnitude smaller. Thus, the numerical effort to simulate 17 shedding cycles on the coarse grid is about 500 times smaller than on the finest grid. The grid sequencing technique takes advantage of this fact by using the established
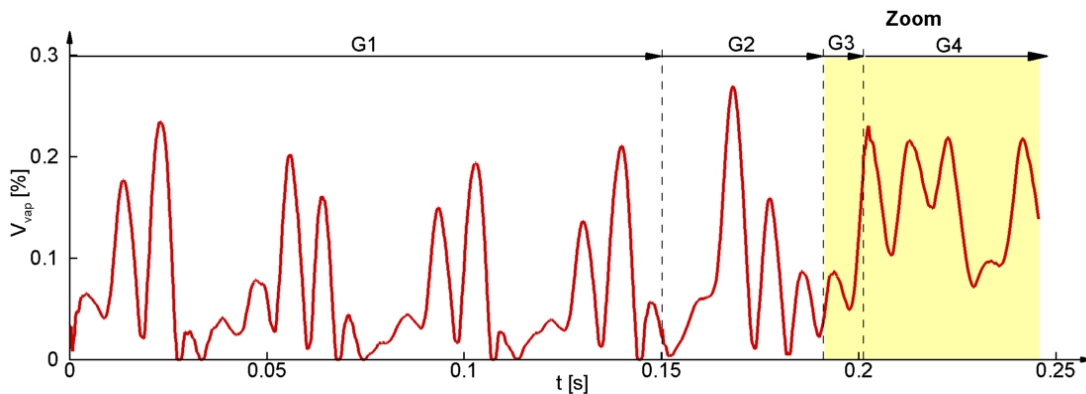

Fig. 2   **Temporal evolution of the total vapor volume content V_{vap} [%] within the computational domain**
Grid sequencing procedure applied to 4 successively refined grids: G1 - $2 \cdot 10^5$ cells (coarse grid), G2 - $4 \cdot 10^5$ cells (medium grid), G3 - $3 \cdot 10^6$ cells (fine grid), G4 - $2.4 \cdot 10^7$ cells (finest/target grid). The coarse grids G1/G2 contain low frequency disturbances that vanish on the finest grid. See **Fig. 3** for detailed information of the simulation on the finest grid G4.
Shedding frequency f≈100 Hz, $\Delta t_{CFD,fine}$=8.5·10^{-8} s.

5

solution obtained for the coarse grid as an improved initial solution for the following finer grids. Thereby, all necessary quantities are interpolated to the next finer grid in a conservative manner and the simulation is continued. Due to the significantly improved initial solution, the simulation of 1 to 5 consecutive shedding cycles is sufficient to obtain an established solution on the finer grid. The process is continued until the finest grid (target grid) is reached. **Figure 3** depicts the zoomed temporal evolution of V_{vap} during the simulated time interval of $\Delta t_{sim} \approx 0.05$ s on the grids G3 (fine) and G4 (finest). The marked time instants correspond to the subsequently analysed flow features. On the finest grid with $2.4 \cdot 10^7$ cells the simulation is performed on 192 processors. The required simulation time to simulate 5 shedding cycles is 4 weeks.

Single-phase reference solution
In order to relate the flow properties of the cavitating flow we calculate a single-phase reference solution of the same numerical set-up, including the same solution algorithm, computational grid (medium grid G2), initial and boundary conditions. We disable the phase transition routines of our numerical method and, hence, the thermodynamic model is given by Eq. (6). We observe a maximum velocity $u_{max}=53.1$ m/s and a minimum pressure coefficient $c_p=-2.37$ (corresponding to a minimum "pressure" of $p_{min}=-6.0$ bar). The numerically predicted drag coefficient is $c_{d,\ num} \approx 10^{-4}$, which is two orders of magnitude smaller than experimentally observed drag coefficients for comparable Reynolds numbers. **As expected, the single-phase flow field is perfectly two dimensional, e.g. the variation of the thermodynamic quantities and of the velocities in spanwise direction is of the order of the numerical round-off error (approx. 10^{-15} for normalized quantities)**.

The steady single-phase solution only depends on the boundary conditions but not on the initial conditions. Moreover, the inviscid single-phase solution is stable - any enforced disturbance damps out and the unique steady solution recovers.

Grid dependence of cavitating flows
Neither the assumed inviscid flow nor the thermodynamic model defines a physical limit of the spatial resolution. However, in practice the resolution is limited by the available hardware resources. The key questions are as follows.
1) Is the model suitable to predict the fragmentation of coherent structures such as clouds and sheets into smaller unities?
2) Are large scale properties such as shedding frequencies and characteristic void fraction distributions (basic shapes of sheet and cloud cavities) grid independent?
3) Provided that 1) and 2) are fulfilled, then how fine has the spatial resolution to be chosen in order to ensure that the desired flow information is resolved?
In order to investigate **1)** and **2)** we analyse the structure of the cavitating flow as obtained during the grid sequencing process. **Figure 4** depicts a comparison of the predicted vapor volume fraction of all four grids. The glossy surfaces are iso-surfaces of the vapor volume fraction $\alpha=0.05$. It is important to note that the depicted flow patterns do not correspond to the same instant in time. The reason therefore is that the applied grid sequencing technique operates consecutively from the coarsest to the finest grid. However, the depicted comparison of the resolved cavitation structures is still representative as it shows corresponding time instants with respect to the shedding process. Our observations are as follows. The simulation predicts the periodic shedding of at least one cloud - independent of the applied computational grid. The shedding frequencies are within a range of $f_{min}=90$ Hz to $f_{max}=107$ Hz. During the first 10 cycles the flow field on the **coarse** grid G1 is essentially two dimensional.

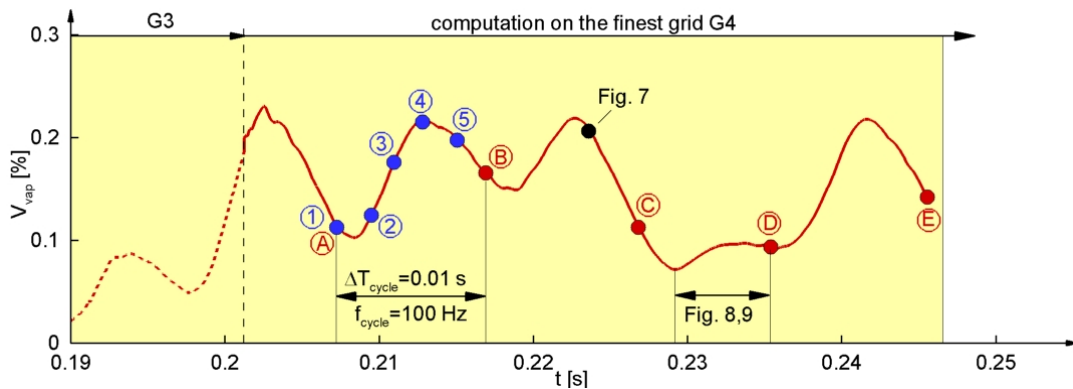Fig. 3   **Zoom of Fig. 2 - total vapor volume [%] versus time - computation on the finest grid G4**
Dots **1** to **5** denote equidistant time instants $\Delta t=2 \cdot 10^{-3}$ s of one shedding cycle with $\Delta T_{cycle}=0.01$ s - see **Fig. 5**.
Dots **A** to **E** denote the break-up of the sheet cavity for 5 consecutive cycles - see **Fig. 6**.
The black dot denotes the time instant analysed in **Fig. 7**, the re-entrant flow analysis is performed within the marked time interval between dots **C** and **D** - see **Fig. 8,9**.
Shedding frequency $f \approx 100$ Hz, $\Delta t_{CFD,fine}=8.5 \cdot 10^{-8}$ s, grid resolution G4 - $2.4 \cdot 10^7$ cells.
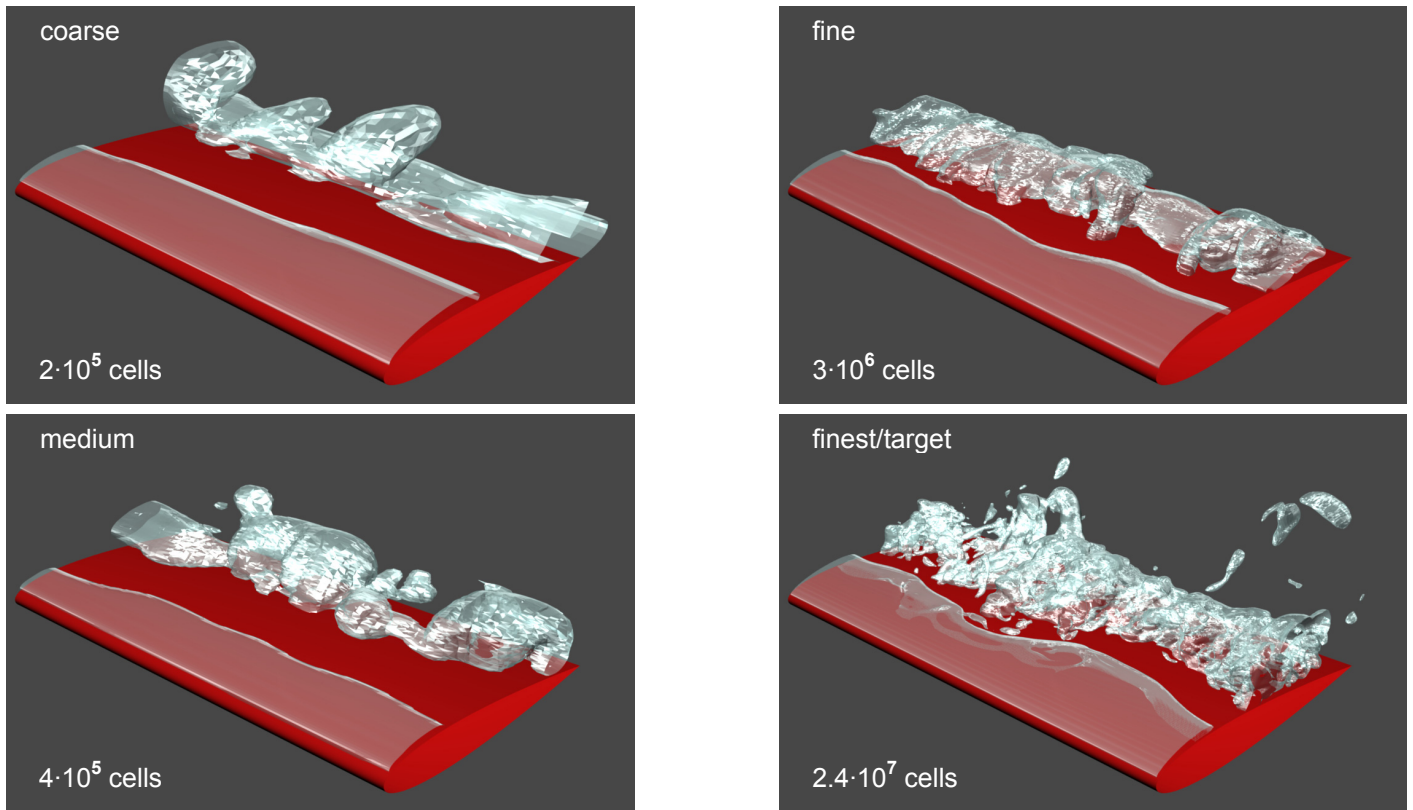
Fig. 4 **Increase of resolved cavitation structures on 4 different computational grids as obtained during grid sequencing**
Perspective view of the hydrofoil and iso-surfaces of the vapor volume fraction α=0.05.
Large scale structures are essentially grid independent, resolved small scale structures (richness of the flow) increases with grid refinement - grid dependence of unsteady cavitating flow. Observed 3-D instabilities are inertia driven (**inviscid** flow model) and develop naturally - self-excited instabilities. Shedding frequency f≈100 Hz, grid resolution G1 (coarse) - $2 \cdot 10^5$ cells, G2 (medium) - $4 \cdot 10^5$ cells, G3 (fine) - $3 \cdot 10^6$ cells, G4 (finest/target) - $2.4 \cdot 10^7$ cells.
NACA 0015, 6° angle of attack, l_{cord}=0.13 m, l_{span}=0.3 m, u_{in}=30 m/s, T_{in}=293 K, p_{exit}=4.5 bar, σ_{ref}=1.0, f_{cycle}≈100 Hz, T_{cycle}≈0.01 s.

After about 10 cycles the first spanwise variation of the shape of the cloud is visible. During a few subsequent cycles the spanwise variation intensifies and reaches a constant order of magnitude (**pic 1** of **Fig. 4**) - a return to a 2-D pattern is not observed. A possible explanation could be that the re-entry flow leads to the onset of the (**inviscid**) Rayleigh-Taylor instability. Thereby, the re-entry flow is lastingly altered in spanwise direction, which results in a non-uniform deformation of the sheet cavity. The first grid sequencing step to the medium grid does not significantly alter the characteristics of the flow field (**pic 2** of **Fig. 4**). The structure of the sheet cavity is still approximately 2-D close to the leading edge, but the richness of the structures within the cloud is slightly increased. The same observation is obtained at the second grid sequencing step to the fine grid. Here, we have to note that the simulation time on the fine grid is supposed to be too short to observe significant differences with respect to the medium grid. However, the last grid sequencing step to the target grid provides new insight into the arising dynamics. Both, the sheet and the cloud contain small scale structures that cannot be resolved on the coarser grids and the 3-D character of the predicted flow is well represented (**pic 4** of **Fig. 4**). The observed rise of small scale structures with increasing spatial resolution motivates the following conclusion. **Unsteady solutions of cavitating flows are typically grid dependent with respect to small scale properties.** However, large scale properties such as shedding frequencies and characteristic void fraction distributions (basic shape of sheet and cloud cavities) seem to be less dependent on the chosen spatial resolution.

Top view - suction side   **Perspective view - suction side**

Fig. 5 **Numerically predicted cavitation structures at time instants 1-5 during the shedding cycle A-B as defined in Fig. 3**
Iso-surfaces of the vapor volume fraction $\alpha=0.05$, top view - left, perspective view - right
Flow: water/water vapor, $u_{in}=30$ m/s, $T_{in}=293$ K, $p_{exit}=4.5$ bar, $\sigma_{ref}=1.0$, $f_{cycle}\approx100$ Hz, $T_{cycle}\approx0.01$ s
Hydrofoil: NACA 0015, 6° angle of attack, $l_{cord}=0.13$ m, $l_{span}=0.3$ m
Simulation: **CATUM**, finest grid G4 $2.4\cdot10^7$ cells, 2nd order in space and time, $\Delta t_{CFD}=8.5\cdot10^{-8}$ s.

Shedding pattern on the target grid

Figure 5 depicts a series of 5 equidistant instants in time of the arising cavitation structures during the shedding cycle **A**-**B** (**Fig. 3**) with $f_{cycle}\approx100$ Hz as observed on the **finest** grid with $2.4\cdot10^7$ cells. The 5 time instants are denoted by blue dots **1**-**5** along the temporal evolution of the vapor volume content V_{vap} in **Fig. 3**. The left column presents the top view of the suction side (**LE**-leading edge, **TE**-trailing edge) and the right column depicts the corresponding perspective view. The glossy surfaces are iso-surfaces of the vapor volume fraction $\alpha=0.05$. Due to different illumination of the iso-surfaces the small scale disturbances of the sheet cavity are clearly visible within the top view but they are less pronounced within the perspective view. At time instant **1** we observe an irregular break-up of the cavity and the formation of cavitating hairpin vortices in streamwise direction. The hairpins connect the larger structures in spanwise direction, both together form crescent shaped regions [15]. At the right hand side, the re-entry flow nearly reaches the leading edge of the foil. The streamwise length of the cavity is $l_{cav}/l_{cord}\approx0.8$ at this instant in time. In accordance with Kawanami at al. [1] we observe a complete separation of the sheet cavity up to its onset close to the leading edge. At time instant **2** the formation of a new sheet cavity is partially visible. The irregular break-up pattern is integrated into a single coherent cloud. At time instant **3** the redeveloped sheet cavity covers roughly one third of the suction side of the hydrofoil. Close to the trailing edge we observe cavitating horseshoe vortices at the end of the downstream travelling cloud. At time instant **4** the downstream part of the sheet cavity is no longer fully attached to the surface of the hydrofoil and the downstream travelling cloud reaches the trailing edge where it fragments and collapses. At time instant **5** the sheet cavity nearly reaches its maximum length and the re-entrant flow is already present.

Comparison of arising break-up patterns

Although the previously described shedding process is periodic with respect to large scale dynamics it varies from cycle to cycle with respect to small scale phenomena. In order to indicate the bandwidth of small scale structures we discuss the break-up patterns for 5 consecutive shedding cycles **A**-**E** as defined within **Fig. 3**. The selected time instants correspond to the same relative position within the shedding process - the instant where the re-entrant flow reaches the onset of the sheet cavity close to the leading edge. **Figure 6** depicts a series of top views of the suction side of the hydrofoil. Glossy surfaces correspond to iso-surfaces of the vapor volume fraction $\alpha=0.05$ and the flow is from top to bottom. The time interval between two successive pictures is $\Delta t=T_{cycle}=0.01$ s. The uppermost picture **A** of **Fig. 6** depicts the break-up pattern of the previously discussed shedding cycle **A**-**B**. The break-up patterns of the following two cycles (**Pics 2** and **3** of **Fig. 6**) contain 5 to 6 crescent shaped regions that occur at approximately the same positions. In cycle 4 we observe a break-up pattern that is biased to the left side of the sheet cavity. This pattern **D** distinguishes from all others as the length of the cavity along the cord is noticeably reduced. The lowermost picture of **Fig. 6** depicts the break-up pattern of cycle 5. **We conclude that the numerically predicted small**

scale structures undergo significant variations from cycle to cycle and the overall flow field is highly 3-D.
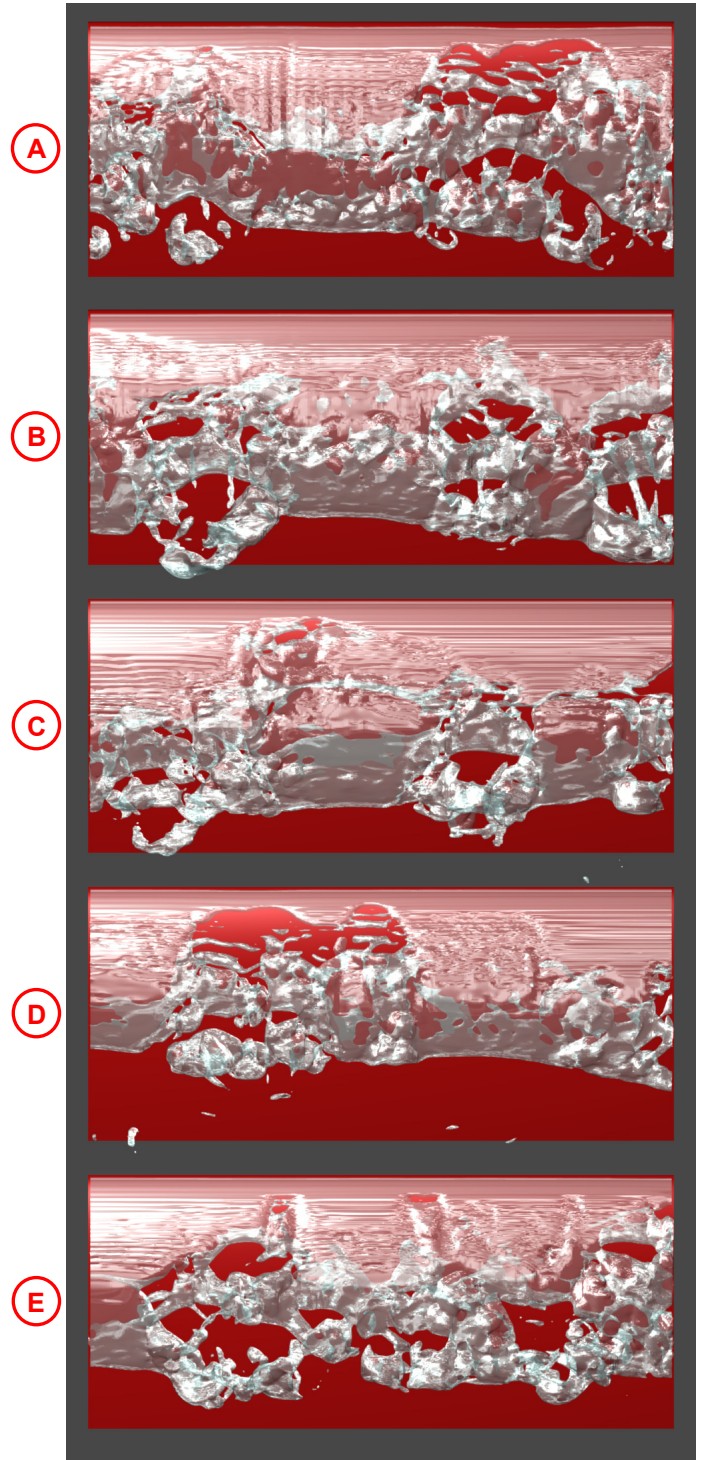

Fig. 6   **Break-up patterns A to E of 5 consecutive shedding cycles**
Top view of the suction side of the hydrofoil at time instants **A** to **E** with $\Delta t_{pic}=T_{cycle}=0.01$ s as denoted with red dots in **Fig. 3**. The selected time instants correspond to the same relative position within consecutive shedding cycles. Iso-surfaces of the void fraction $\alpha=0.05$ demonstrate the occurrence of irregular break-up patterns including hairpin vortices and crescent shaped regions. Finest grid G4 - $2.4\cdot10^7$ cells, $\Delta t_{CFD}=8.5\cdot10^{-8}$ s.

The predicted inner structure of a cloud

Figure 7 provides further insight into the arising small scale structures within a typical sheet and cloud cavitation pattern at one instant in time - see **Fig. 3**. We define the analysis plane A-A, which is indicated within the top view of the suction side of the hydrofoil (**Fig. 7** - top). The corresponding vapor volume fraction α within this plane is depicted at the bottom of **Fig. 7**. As expected, the void fraction α is approximately uniform within the sheet cavity. However, the downstream travelling cloud contains a significantly non-uniform distribution of the void fraction. The results of our simulations indicate that this non-uniformity is mainly due to superposition of cavitating vortices during the formation of the cloud. The inhomogeneity of the void fraction distribution and of the velocity field plays an important role at the stage of the cloud collapse. We observe that regions with low values of the void fraction partially condense during the advection of the cloud downstream to the trailing edge. The resulting fragmentation into smaller cloud structures lead to a series of violent cloud collapses including the formation and propagation of shocks with instantaneous pressure rises of up to 2400 bar. These shocks are known to be a driving mechanism of cavitation erosion. Moreover, they enforce total pressure losses, vorticity production and further alternation of the flow field.
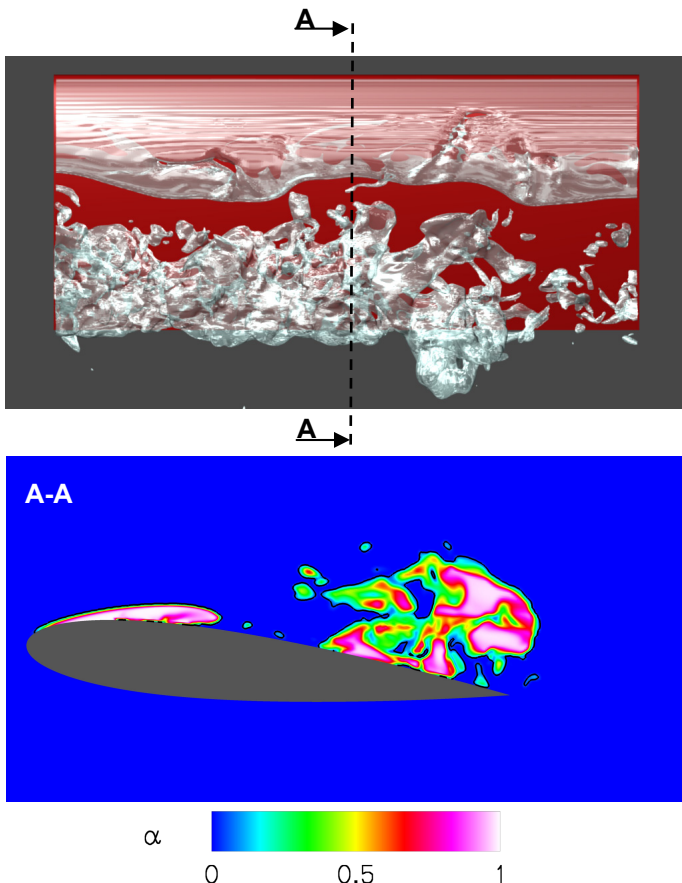

Fig. 7   Inner structure of the cavity
Top - typical sheet and cloud cavitation on the suction side of the hydrofoil, iso-surfaces of the void fraction α=0.05.
Bottom - void fraction α at plane A-A indicating the complex inner structure of the flow within the cloud.
Time instant is marked within **Fig. 3**.
Finest grid G4 - $2.4 \cdot 10^7$ cells, Δt_{CFD}=$8.5 \cdot 10^{-8}$ s.

Analysis of re-entry flow

In this section we analyse the shedding process as it is predicted by the applied model. It is important to review that the model is based on the assumptions of inviscid and adiabatic flow and equilibrium thermodynamics within each computational cell. It can be shown that these assumptions imply that the total entropy remains constant along each particle path **as long as the flow is continuous (shock free). However, the model predicts a discontinuous recondensation at the closure region of the sheet cavity. The states on both sides of the discontinuity fulfill the Rankine-Hugoniot conditions as known from gasdynamic shocks. We observe a maximum total pressure loss of up to 70% close to the surface of the hydrofoil and significant formation of vorticity. Figure 8** depicts a series of 5 instants in time with time intervals Δt_{1-2}=$2.5 \cdot 10^{-3}$ s, Δt_{2-3}=$1.5 \cdot 10^{-3}$ s, Δt_{3-4}=$1.0 \cdot 10^{-3}$ s and Δt_{4-5}=$1.0 \cdot 10^{-3}$ s. The complete time interval Δt_{1-5} is marked in **Fig. 3**. The left column contains the vapor volume fraction α within the plane A-A as defined in **Fig. 7**. The right column shows the corresponding x component of the velocity. At the first time instant a recently developed sheet cavity nearly reaches the position of the thickness maximum of the hydrofoil. The sheet undergoes further growth along the cord of the hydrofoil and its closure region steepens up. The x component of the velocity within the sheet is $u_1 \approx 44$ m/s and the static pressure is the vapor pressure. At time instant **2** the sheet cavity consists of two portions, an attached upstream part and a detached downstream part. The upstream part of the sheet is no longer growing - its position on the surface of the hydrofoil is frozen for a short time. At the end of the upstream part, particularly close to the surface of the hydrofoil, we observe a discontinuous variation of the void fraction and of the x component of the velocity u_1 (black arrow in **pic 2** of **Fig. 8**). This is the position where significant vorticity production is observed - see subsequent section and **Fig. 9**. The velocity directly downstream of the discontinuity is nearly zero but further downstream a re-entry jet is already present and reaches a value of $u_1 \approx -5$ m/s of the x component of the velocity. The downstream part of the sheet is still growing along the spanwise direction. At time instant **3** the reverse flow covers roughly one third of the thickness of the downstream part of the sheet ($\delta_{re-entrant} \approx 3$ mm). The x component of the velocity of the re-entrant jet is $u_1 \approx -20$ m/s close to the end of the downstream part. Additionally, the two parts of the sheet are no longer directly linked together - the downstream part is from now on termed as cloud. The discontinuous transition at the end of the upstream part moves towards the leading edge with $u_1 \approx -7$ m/s (position of black arrow in **pics 3,4** of **Fig. 8**). At time instant **4** the maximum thickness of the re-entry flow is $\delta_{re-entrant} \approx 7$ mm and the x component of the velocity is $u_1 \approx -30$ m/s. The remaining attached sheet terminates slightly upstream to the thickness maximum of the hydrofoil and the cloud starts to grow in height. At time instant **5** the previously attached sheet forms another cloud as the re-entry flow reaches the onset position of the cavity close to the leading edge. The maximum value of the x component of the velocity of the re-entry flow at this instant in time is $u_1 \approx -52$ m/s.
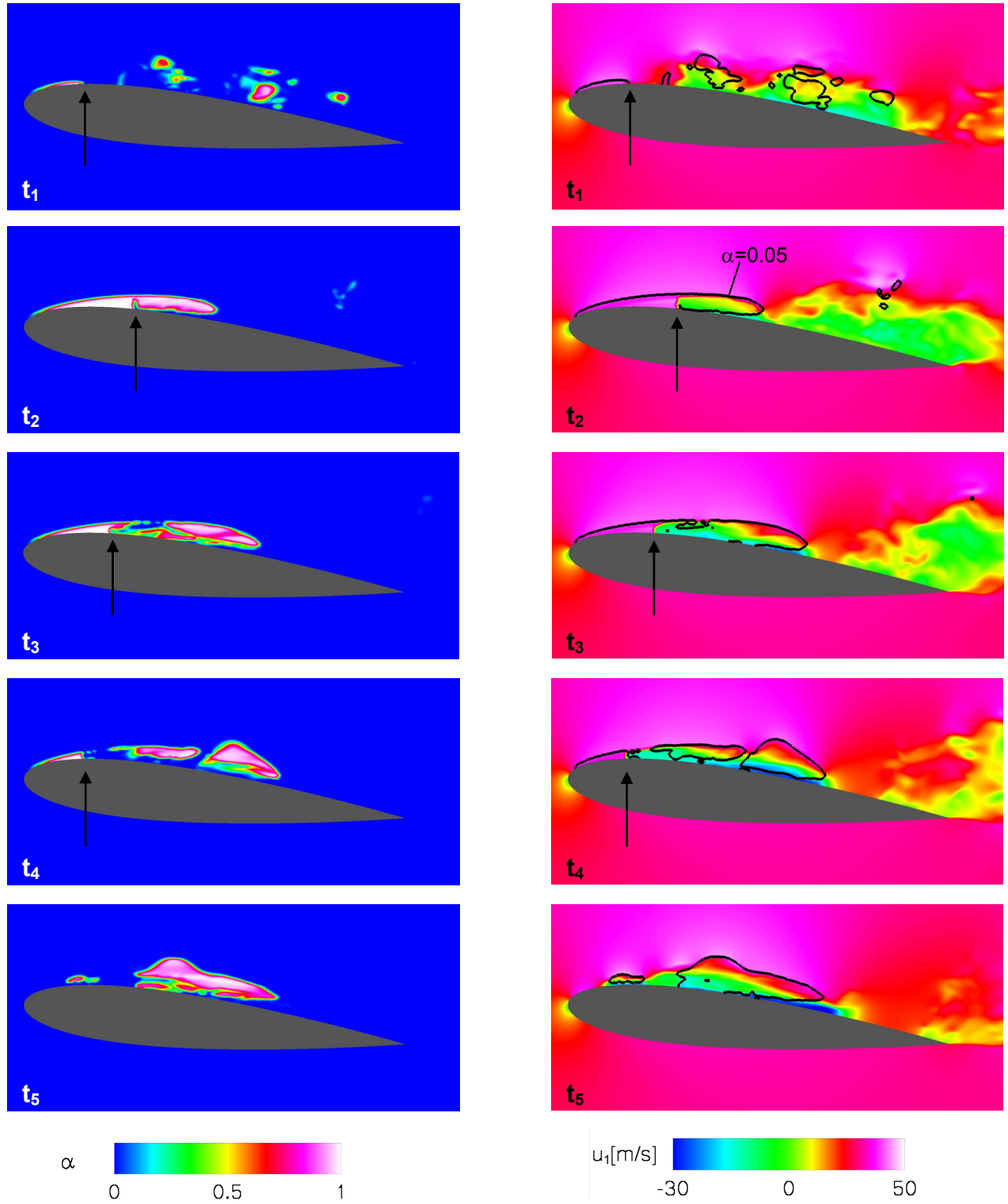
Fig. 8   **Development and subsequent separation of a sheet cavity - analysis of the re-entrant jet**
left   void fraction α at 5 instants in time with intervals $\Delta t_{1-2}=2.5 \cdot 10^{-3}$ s, $\Delta t_{2-3}=1.5 \cdot 10^{-3}$ s, $\Delta t_{3-4}=1.0 \cdot 10^{-3}$ s, $\Delta t_{4-5}=1.0 \cdot 10^{-3}$ s.
right   x component of the velocity u_1 corresponding to t_1 - t_5, black isolines correspond to the void fraction $\alpha=0.05$.
The time interval t_1 - t_5 is indicated within **Fig. 3**. Arrows point to the attached part of the sheet where the discontinuity appears.
Finest grid G4 - $2.4 \cdot 10^7$ cells, $\Delta t_{CFD}=8.5 \cdot 10^{-8}$ s.

Vorticity production due flow discontinuities

As stated in the previous section, the predicted formation of vorticity is due to the discontinuous condensation at the closure region of the sheet during the growth process and during the collapse of the cavity. Hence, the flow is strongly rotational even before the re-entrant jet and the shedding mechanism become relevant. **Figure 9** corresponds to the same instant in time as **pic 2** of **Fig. 8**. The upper picture shows iso-surfaces of the vapor volume fraction $\alpha=0.05$ on the suction side of the hydrofoil. The lower one depicts iso-surfaces of the magnitude $|\omega|=10^4$ 1/s of the vorticity vector. It is observed that the onset of strong vorticity is located within the sheet cavity, precisely at that location where the attached part of the cavity recondenses. The growth of the detached part of the sheet results in the advection of the vorticity along the hydrofoil (smooth iso-surface of **Fig. 9**). The fragmentation of the sheet and the subsequent cloud shedding alters the flow field and leads to a rich vortical flow pattern. It is obvious that such pronounced 3-D characteristics result in highly 3-D cavitation structures as observed and discussed within this investigation.

Shock induced maximum loads

The collapse of a cloud or of a small structure within a cloud enforces the acceleration of the surrounding liquid towards the center of the cloud, comparable to the flow field of an isolated sink. At the instance of the final collapse, a significant part of the kinetic energy of the surrounding liquid is transferred to the formation of a shock, which leads to the discontinuous deceleration of the velocity towards the center of the cloud. The approximately spherical shock front propagates with a velocity $u_S \approx 1500$ m/s through the liquid. Due to the rise of the pressure behind the shock, the collapse of surrounding clouds/bubbles is initiated or intensified. With respect to cavitation erosion this process is especially important if it takes place close to the surface of the hydrofoil. The CFD-Tool **CATUM** enables the simulation of shock formation and propagation [9-14] and provides a prediction of shock induced maximum loads on the surface of the hydrofoil. The key idea is to record the static pressure within all computational cells that are located at the surface of the hydrofoil for the time interval $\Delta t_{A-E}=0.04$ s as denoted within **Fig. 3**. The computational cells at the surface of the hydrofoil are thus interpreted as pressure transducers. The corresponding sampling frequency of the numerical transducers is $f_{sample} \approx 10^7$ Hz, the average area of each of the numerical transducers is 0.5 mm x 1.2 mm = 0.6 mm². Those positions where the highest pressure peaks are recognized provide an indication of erosion sensitive areas. **Figure 10** depicts an output of the numerical transducers. For each computational cell at the surface of the hydrofoil the maximum pressure during the time interval $\Delta t_{A-E}=0.04$ s is determined and visualized. We observe instantaneous maximum loads of 2400 bar close to the trailing edge of the hydrofoil. It should be noted that the analysed time interval $\Delta t_{A-E}=0.04$ s is extremely short compared to experimental investigations [16] on cavitation erosion. However, our previous investigations [13,14] indicate that 5 to 10 shedding cycles provide sufficient data to determine the locations where erosion is most likely to occur.
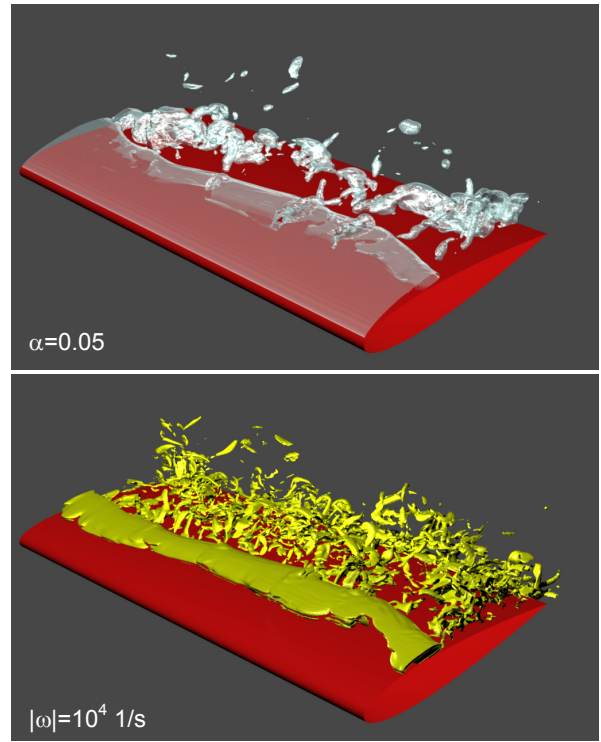

α=0.05

|ω|=10⁴ 1/s

Fig. 9   Correlation of void fraction α and vorticity $|\omega|$
Iso-surfaces of the vapor volume fraction $\alpha=0.05$ (top) and iso-surfaces of the magnitude $|\omega|=10^4$ 1/s of the vorticity vector (bottom) on the suction side of the hydrofoil. The corresponding time instant t_2 is defined in **Fig. 8**.
Finest grid G4 - $2.4 \cdot 10^7$ cells, $\Delta t_{CFD}=8.5 \cdot 10^{-8}$ s.
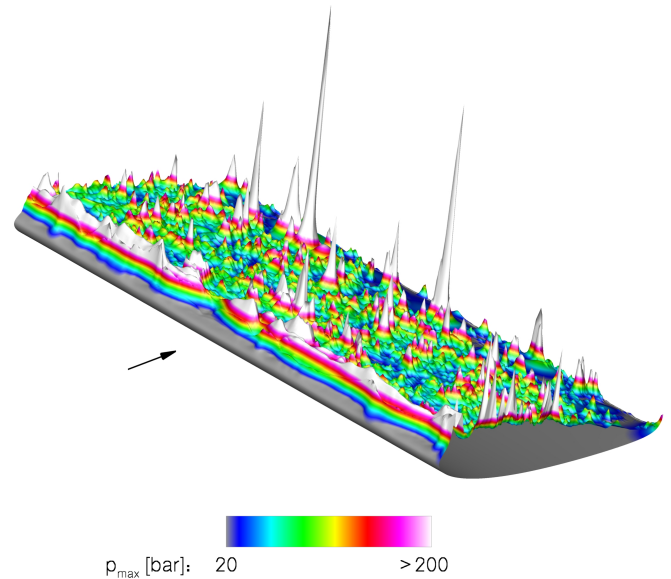

p_{max} [bar]:   20   > 200

Fig. 10   Instantaneous maximum loads
Analysis of occurring maximum pressure within each computational cell at the suction side of the hydrofoil during the analysis interval **A** to **E** with $\Delta t_{A-E}=0.04$ s as defined in **Fig. 3**. The maximum pressure at the trailing edge is $p_{max}=2400$ bar.
Finest grid G4 - $2.4 \cdot 10^7$ cells, $\Delta t_{CFD}=8.5 \cdot 10^{-8}$ s.

CONCLUSION

The investigation focuses on wave and inertia driven mechanisms of cavitating flows. We apply the CFD-Tool **CATUM** (**CA**vitation **T**echnische **U**niversität **M**ünchen) to simulate the 3-D flow around a 2-D hydrofoil with special emphasis on self-excited instabilities in spanwise direction. It is demonstrated that these instabilities are predictable by the assumption of inviscid flow and equilibrium thermodynamics. The importance of sufficient resolution in space and time is analyzed by a grid dependence study. Large scale characteristics are only weakly dependent on the resolution while small scale structures are strongly grid dependent. The simulation predicts various irregular break-up patterns, hairpin and horseshoe vortices. These delicate features of the flow vary from cycle to cycle, strong periodicity is not observed for the investigated set-up. The development of the re-entry jet as part of the shedding mechanism is analyzed. Here, we observe significant vorticity production during the growth and the collapse of the sheet cavity. It is demonstrated that the vorticity production is caused by a discontinuity at the end of the attached part of the cavity where condensation takes place. The discontinuity fulfills Rankine-Hugoniot conditions as known from gasdynamic shocks. Contrary to the discontinuity related with the formation and break-up of the sheet cavity, we observe shocks due to collapsing fragments of clouds. These shocks produce significant maximum loads of $p_{max} \approx 2400$ bar, particularly close to the trailing edge of the investigated hydrofoil. We conclude that the dynamics of sheet and cloud cavitation are essentially inertia controlled. Hence, the application of an inviscid flow model to simulate cavitating flows is justified - provided that it is ensured that the boundary layers of the corresponding single-phase flow remain attached.

ACKNOWLEDGMENTS

NOMENCLATURE

u, u_i	velocity, velocity components
c	speed of sound
M	Mach number
$\bar{q}$	vector of conserved quantities
$F_i(\bar{q})$	flux-vector in direction x_i
ρ	density
$\rho_{v,sat}$	saturation vapor density
$\rho_{l,sat}$	saturation liquid density
E	mass specific total energy
e	mass specific internal energy
U	total internal energy
p	static pressure
T	static temperature
α	vapor volume fraction
ε	vapor mass fraction
σ_{ref}	cavitation number
x_i	coordinate direction
Δt_{CFD}	numerical time step
V_{vap}	integrated vapor volume [%]
f	frequency
l_{cord}	cord length
l_{span}	span width
$l_{cav,c}$	length of the cavity along the cord
$l_{cav,s}$	spanwise length of a shedded cloud
$\delta_{re-entrant}$	thickness of re-entrant jet

REFERENCES

[1] Kawanami, Y., Kato, H., Yamaguchi, H. 1998, "*Three-Dimensional Characteristics of the Cavities Formed on a Two-Dimensional Hydrofoil*", Proceedings CAV1998 - Third International Symposium on Cavitation, Grenoble, France, pp. 191-196, 1998.

[2] Franc, J. P., 2001, "*Partial Cavity Instabilities and Re-Entrant Jet*", Invited Lecture, Proceedings CAV2001 - Fourth International Symposium on Cavitation, Pasadena, USA, CD- ROM publication, 2001.

[3] Franc, J. P., Michel, J. M. 2004, "*Fundamentals of Cavitation*", Kluwer Academic Publishers, Fluid Mechanics and its Applications, Volume 76, ISBN 1-4020-2233-6, p. 134, 2004.

[4] Trevena, D. H. 1984, "*Cavitation and the Generation of Tension in Liquids*", J. Phys. D: Appl. Phys., Vol. 17, pp. 2139-2164, 1984.

[5] Delale, C. F., Okita, K., and Matsumoto, Y. 2005, "*Steady-State Cavitating Nozzle Flows with Nucleation*", J. Fluids Eng., Vol. 127, pp. 770-777, 2005.

[6] IAPWS, International Association for the Properties of Water and Steam, www.iapws.org, "*The IAPWS Industrial Formulation 1997 for the Thermodynamic Properties of Water and Steam*", ASME J. Eng. Gas Turbines and Power, **122**, 150-182, 2000.

[7] Saurel, R., Cocchi, J. P., and Butler, P. B. 1999, "*Numerical Study of Cavitation in the Wake of a Hypervelocity Projectile*", J. Propulsion and Power, Vol. 15, No. 4, pp. 513-522, 1999.

[8] Oldenbourg, R. 1989, "*Properties of Water and Steam in SI-units*", Springer-Verlag, Berlin, 1989.

[9] Schnerr, G. H., Schmidt, S. J., Sezal, I. H., and Thalhamer, M. 2006, "*Shock and Wave Dynamics of Compressible Liquid Flows with Special Emphasis on Unsteady Load on Hydrofoils and on Cavitation in Injection Nozzles*", Invited Lecture, Proceedings CAV2006 - Sixth International Symposium on Cavitation, CD- ROM publication, 2006.

[10] Schmidt, S. J., Sezal, I. H., Schnerr, G. H., and Thalhamer, M. 2008, "*Riemann Techniques for the Simulation of Compressible Liquid Flows with Phase-transition at all Mach numbers - Shock and Wave Dynamics in Cavitating 3-D Micro and Macro Systems*", Proceedings 46th AIAA Aerospace Sciences Meeting and Exhibit, Nevada, USA, AIAA paper 2008-1238, 2008.

[11]   Schnerr, G. H., Sezal, I. H., Schmidt, S. J. 2008, "*Numerical Investigation of Three-dimensional Cloud Cavitation with Special Emphasis on Collapse Induced Shock Dynamics*", Physics of Fluids, Vol. 20, Issue 4, 2008.

[12]   Schmidt, S. J., Sezal, I. H., Schnerr, G. H., and Thalhamer, M. 2007, "*Shock Waves as Driving Mechanism for Cavitation Erosion*," Proceedings ISAIF - International Symposium on Experimental and Computational Aerothermodynamics of Internal Flows, edited by I. Trebinjak, CD-ROM publication, 2007.

[13]   Schmidt, S. J., Thalhamer, M., Schnerr, G. H. 2009, "*Density Based CFD Techniques for Simulation of Cavitation Induced Shock Emission*," Proceedings ETC - 8th European Turbomachinery Conference, Graz, Austria, pp. 197-208, 2009.

[14]   Sezal, I. H., Schmidt, S. J., Schnerr, G. H., and Thalhamer, M. 2009, "*Shock and Wave Dynamics in Cavitating Compressible Liquid Flows*", Shock Waves, DOI 10.1007/s00193-008-0185-3, 2009.

[15]   Reisman, G. E., Wang, Y. -C., and Brennen, C. E. 1998, "*Observations of Shock Waves in Cloud Cavitation*", J. Fluid Mech., Vol. 355, pp. 255-283, 1998.

[16]   Huber, R. 2004, "*Geschwindigkeitsmaßstabseffekte bei der Kavitationserosion in der Scherschicht nach prismatischen Kavitatoren*", Report Nr. 102, Lehrstuhl und Versuchsanstalt für Wasserbau und Wasserwirtschaft, TU München, Munich, Germany, 2004.